On rebuilding landslide parameters from long-period seismic waveform inversion

Xiao Wang[1], Xinghui Huang[1, 2*], Po Chen[2], Lei Xu[3], Heng Wang[4], Wenze Deng[1], Dan Yu[1], Zhengyuan Li[1], Qiang Xu[5]

[1]China Earthquake Networks Center, Beijing, China

[2]Department of Geology and Geophysics, University of Wyoming, Laramie, United States

[3]The 7th Institute of Geology & Mineral Exploration of Shandong Province, Linyi, China

[4]Center for Economic Geology Research, University of Wyoming, Laramie, Wyoming, United States

[5]State Key Laboratory of Geohazard Prevention and Geoenvironment Protection, Chengdu University of Technology, Chengdu, China

Corresponding author: Xinghui Huang (huangxh19850216@gmail.com)

Key Points:

- We propose an approach to determine the frequency band required by the inversion to reliably reconstruct landslide movement parameters
- We perform a long-period seismic waveform inversion for the 2003 Qianjiangping landslide
- We discuss effects of mass entrainment during sliding on rebuilding landslide movement parameters

Abstract

Landslide force history inverted from long-period seismic records for a landslide has been used to extract its physical parameters. An important precondition is that the inverted landslide force histories are reasonable approximations. We first discuss how to estimate the accuracy of the inverted force histories and then propose an approach to determine the proper frequency band used in the inversion. We perform a long-period seismic waveform inversion for the 2003 Qianjiangping landslide to obtain its force time history and estimate its movement parameters. Based on the results, we build a simple model to study the effects of the portion of the initial sliding mass and the location of the mass entrainment on the seismically estimated mass, which shows that if the entrainment occurs at the slow-down phase the seismically estimated mass is a closer approximation of the initial sliding mass.

Plain Language Summary

A landslide is a dynamic process that occurs on the surface of the earth. The force exerted on the earth's crust during the occurrence is propagated in the form of seismic waves and recorded by the seismic station, which can be used to estimate the kinematics and dynamics of the landslide. The difference of the parameters used in obtaining the force sequence leads to different results for the same event, and the understanding and interpretation of the event are also affected. In this study, we discussed what kind of results are relatively reasonable and how to choose parameters to get them. Besides, the driving force of the initial sliding is gravity, which can be monitored by the earth's crust; during the sliding, the driving force of the passively moving material is from the material that is already in motion, and this force cannot be detected. We used a simple model to show the effect on the inversion results when the mobilized material is located at different positions on the sliding path. The simulation shows that if the material is entrained at the slow-down phase, the seismically estimated mass is closer to the initial sliding mass.

1. Introduction

Landslide force history inversion using long-period seismic records based on a Single-Force source model [e.g., *Dahlen*, 1993; *Fukao*, 1995; *Hasegawa and Kanamori*, 1987; *Kanamori and Given*, 1982; *Kanamori et al.*, 1984] and a fixed point source assumption has been widely adopted to study landslide kinematics [e.g., *Allstadt*, 2013; *Ekström and Stark*, 2013; *Gualtieri and Ekström*, 2018; *Hibert et al.*, 2014; *Hibert et al.*, 2015; *W Li et al.*, 2019; *Moore et al.*, 2017; *Moretti et al.*, 2015; *Sheng et al.*, 2020; *Yamada et al.*, 2013; *Zhao et al.*, 2020]. The algorithms used in previous studies, although not exactly the same in detail due to implementation strategies by individual researchers, are proven to be robust. The authors of the present study have also developed an algorithm to invert for landslide force histories and have successfully applied it to the Wulong landslide [*Li et al.*, 2017], the Xinmo landslide [*Z-y Li et al.*, 2019], and the Xiaoba landslide [*Yu et al.*, 2020].

Based on the inverted landslide force histories, relationships between the maximum inverted forces and sliding volumes can be derived and such relationships can be used to estimate sliding volumes in future landslide studies [*Chao et al.*, 2016; *Ekström and Stark*, 2013]. Landslide basal frictions are either estimated directly by adopting a block model [e.g., *Allstadt*, 2013; *Brodsky et al.*, 2003; *Yamada et al.*, 2013; *Zhao et al.*, 2015] or obtained from a joint analysis with numerical landslide simulations [*Moretti et al.*, 2015; *Moretti et al.*, 2012; *Yamada et al.*, 2016; *Yamada et al.*, 2018]. An important precondition for the above interpretation work is that the inverted landslide force histories are reasonable approximations. However, at least two important factors that affect the quality of the interpretation work are rarely discussed in previous studies. The first one is how to choose a proper frequency band to carry out the force-history inversion; and the second one is how mass entrainments during sliding affect the estimated parameters during interpretation.

In this paper, we first discuss how to estimate the accuracy of the inverted force histories and then propose an approach to determine the proper frequency band used in the inversion in order to rebuild landslide movement parameters from inverted force histories. We demonstrate our approach using the Qianjiangping landslide that occurred in 2003. Using the force history obtained by inverting long-period seismic waveform data, we build a model to study the effects of the portion of the initial sliding mass and the location of the mass entrainment on the estimated mass and other interpretation parameters.

2. The Qianjiangping Landslide and Seismic Observations

The catastrophic Qianjiangping landslide occurred at approximately 16:20:00 UT on July 13, 2003. It had a volume of about 2.04×10^7 m^3 and caused substantial economic loss. It was located on the left bank of the Qinggan River within the Three Gorges Reservoir area. The river bends in front of the Qianjiangping slope and the erosion at the toe of the slope caused by the river is believed to have had a negative impact on the slope stability. As shown in Figure 1, the landslide had a tongue-like shape in map view, with a length of ~1,200 m and a width of ~1,000 m. It moved

~250 m in the main sliding direction of S45°E [*Wang et al.*, 2008]. The Qianjiangping landslide consisted of a main sliding area and a collapsed area. The toe of the main sliding area slid into the Qinggan River, blocking the flow. On the contrary, the collapsed area was just drawn down by the movement of the main sliding area with a very limited sliding distance [*Wang et al.*, 2008].

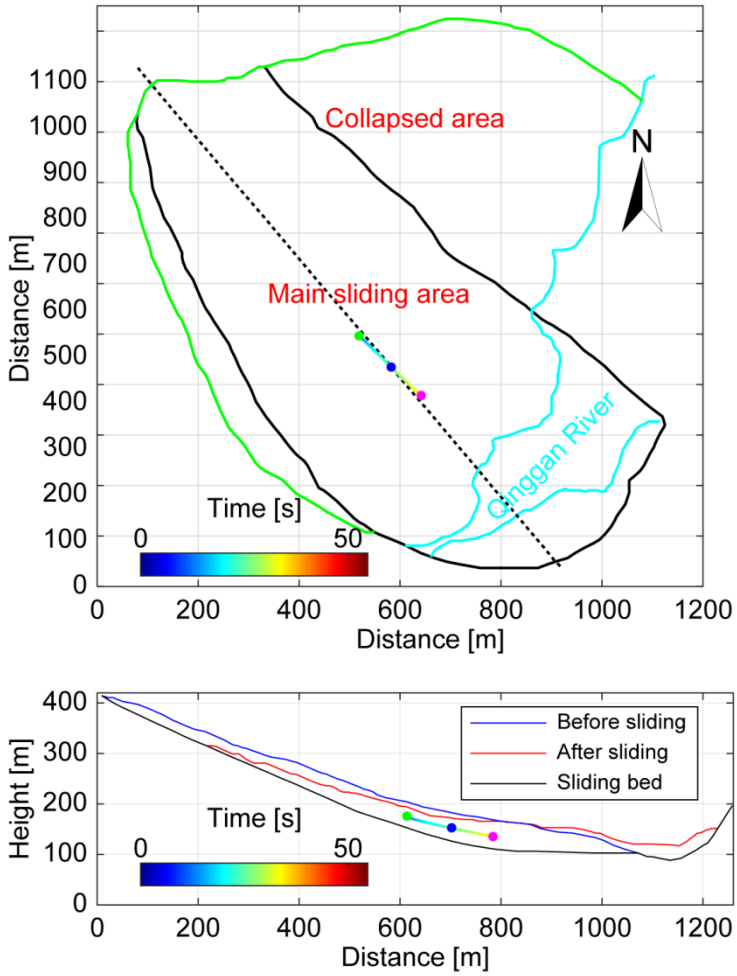

Figure 1. Map (upper panel) and central longitudinal section (lower panel) of the Qianjiangping landslide (adapted from [*Wang et al.*, 2008]).

We collected seismic records for this landslide event at seismic stations within an epicentral distance of ~10 degrees. The locations of the seismic stations are shown in Figure S1. The nearest seismic station was ENH with an epicentral distance of ~131.6 km. Figure S2 shows the East-West component seismic records at the ENH station within different frequency bands. The start time of the low-frequency waveform associated with the landslide event is much earlier than that of the high-frequency waveform. High-frequency seismic signals appeared close to the end of the event. With the appearance of the high-frequency seismic signal, there appeared a short-duration, energetic pulse on the low-frequency waveform.

Since high frequency energy decays rapidly with distance, it was only detected

by the nearest two seismic stations. On the other hand, low-frequency seismic energy could be detected by seismic station as far as ~1000 km (Figure S3). Seismic recordings at three coastal stations, SSE, KMNB, and MATB, had relatively poor signal-to-noise ratios. Recordings at MATB were too noisy and were not plotted in Figure S3. Recordings at SSE had very small amplitudes. The arrival times at SSE and KMNB were ~70 seconds later than those at other stations of similar epicentral distances, which is likely due to differences in seismic velocities along different source-station paths.

3. Landslide Force History Inversion

A robust force-history inversion should at least meet two levels of requirements. First, the entire inversion workflow, consisting of seismic data processing, calculation of the Green's functions, the implementation of the solution algorithm, should be mathematically correct. A typical sign of reaching this level of requirement is a reasonable match between the recorded seismic waveforms and the corresponding synthetic waveforms, sometimes quantified using certain goodness-of-fit measurements. At the current stage, the majority of force-history inversion studies can meet this level of requirements.

The second level of requirements is associated with physical feasibilities, i.e., the dynamic and kinematic parameters inferred from the inverted force histories should be within reasonable ranges given by the physical processes of the landslide. For example, inferred sliding trajectories should be generally consistent with actual sliding traces of the mass center. The frequency band of the seismic data used in the inversion can have a substantial impact. For example, force histories of the Bingham Canyon Mine landslides inverted using seismic data within different frequency bands had nonnegligible differences not only in amplitudes but also in the shape and the duration [*Hibert et al.*, 2014; *Moore et al.*, 2017; *Zhang et al.*, 2020]. It is unlikely that all of the inverted force histories were physically feasible.

It has been recognized that the long-period seismic signals used in landslide force history inversions are generated by unloading and reloading of the solid earth while the sliding mass accelerates and decelerates [e.g., *Chao et al.*, 2016; *Ekström and Stark*, 2013; *Hibert et al.*, 2014; *Hibert et al.*, 2015]. Therefore, to rebuild the acceleration/deceleration history of a sliding mass, the seismic waveform data used in the inversion must have a duration that fully covers the duration of the acceleration/deceleration process. Specifically, if the longest duration of the acceleration/deceleration processes is T, the lowest frequency of the seismic waveform data should be no larger than $1/2T$ Hz. Normally, a landslide contains one major acceleration phase and one major deceleration phase. In practice we estimate the low frequency bound of the passing band using the whole duration of the sliding event by assuming the same duration of the acceleration and deceleration phases.

In practice, we usually do not know the duration of the sliding event prior to the force-history inversion. However, the duration of the low-pass filtered seismic

waveforms at the nearest seismic station provides a reasonable approximation of the duration of the sliding event. For the Qianjiangping landslide, the waveform at the nearest station (Figure S3) shows that the duration of the sliding event was ~66 s. We therefore set the lower bound of the frequency band used in our landslide force history inversion at 0.015 Hz. Seismic signals below this lower frequency bound should be removed thorough filtering since they are unrelated to the sliding event and may contaminate the force-history inversion results. It should be noted that commonly used filters usually have transition bands around corner frequencies, which can potentially distort the signals in the passing band. An example of the amplitude response of a 4^{th}-order 0.01 – 0.1 Hz Butterworth band-pass filter is shown in Figure 2. Signals between the low-frequency bound and the corner frequency (shaded area in Figure 2), is distorted. For the Xinmo landslide, this distortion may explain why *Z-y Li et al.* [2019] can rebuild a reasonable sliding trajectory, while the trajectory of *W Li et al.* [2019] shows a circle-back, even though both studies used the same low-frequency bound in seismic data processing.

The high-frequency bound should be determined by considering two factors: small-scale features in the landslide source that we would like to resolve and heterogeneities in elastic media along source-station paths that we can account for in the Green's functions. Errors in the inverted force histories due to high-frequency seismic noises are usually concentrated in high-frequency bands and their influences on the reconstruction of the sliding trajectories through integration over time are usually negligible. However, they may lead to misidentification or mischaracterization of small-scale landslide mass movements. In our study of the Qianjiangping landslide, we used a flat-layered velocity model derived from Crust 1.0 and the Green's functions were computed using the matrix propagation method of *Wang* [1999]. The velocity model and the resulting Green's functions are accurate below 0.1 Hz for stations within ~500 km epicentral distance (i.e., station ENH and XAN). Therefore, the high-frequency bound of our band-pass filter was set to 0.1 Hz. The band-pass filtered seismic waveforms were then used in our inversion, which was carried out in the frequency domain to improve computational efficiency.

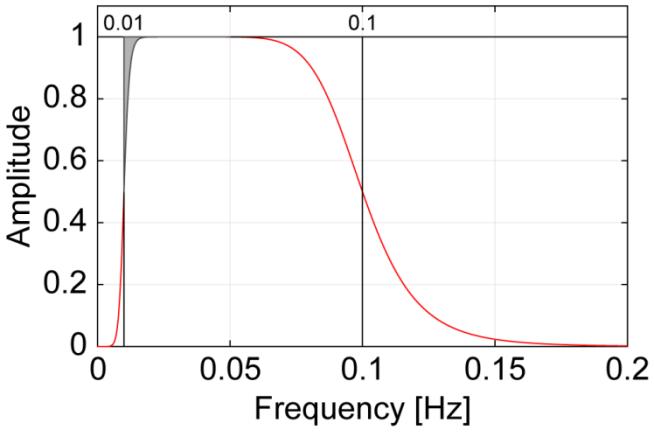

Figure 2. Amplitude response of a non-causal fourth-order 0.01 – 0.1 Hz Butterworth bandpass filter.

In general, synthetic waveforms computed from the inverted force histories show excellent fit with the corresponding observed waveforms (Figure S4), suggesting that our inversion result likely meets the first level of requirement. From the inverted landslide force history shown in Figure 3, we recognize that the landslide started at ~16:19:42.2 with a duration of ~54.8 s. The maximum absolute force reached ~2.1×10^{10} N. When determining the start and end times for a landslide, we usually choose the times closest to zero forces, such as those denoted using green dashed lines in Figure 3. We call them *apparent* start and end times. However, if we carefully observe the force curves, it might be more reasonable to define an earlier start time and a later end time as denoted using red dashed lines in Figure 3. We call them *real* start and end times. Force curves show an overall deviation from zero before the real start time and slow energy decay after the real end time. We believe this phenomenon is caused by filtering. Seismic waveform data are commonly filtered using a non-causal band-pass filter before being used in the inversion, which is equivalent to apply the same filter to the inverted force history. The filtering operation could potentially modify the shape of the inverted force history by shifting values of the start and end times from the baseline.

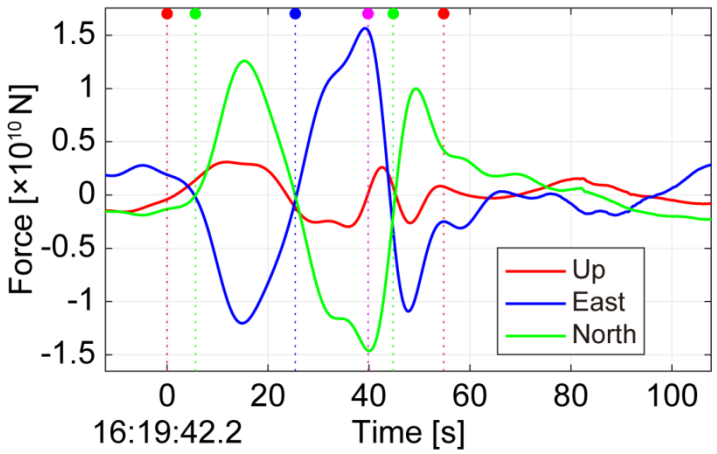

Figure 3. Inverted force history for the Qianjiangping landslide. Red dashed lines, green dashed lines, the blue dashed line, and the magenta dashed line denote the real start and end times, apparent start and end times, the maximum velocity time, and the maximum displacement time, respectively.

4. Landslide dynamics

Based on Newton's third law of motion, the forces acting on the sliding mass can be obtained by multiplying the inverted force history by -1 [e.g., *Gualtieri and Ekström*, 2018; *Kanamori and Given*, 1982; *Yamada et al.*, 2013]. We can then use this force to either calculate velocity and displacement distributions of the sliding

material for a given mass [e.g., *W Li et al.*, 2019; *Z-y Li et al.*, 2019; *Yu et al.*, 2020] or estimate the sliding mass by minimizing the discrepancies with the sliding trajectories from satellite images [e.g., *Hibert et al.*, 2014]. We adopted the second approach and estimated the sliding mass to be ~2.1655×10^{10} kg by minimizing the discrepancies with the trajectories of the sliding material weight center from *Wang et al.* [2008], which is shown in Figure 1. Both the recovered horizontal and vertical trajectories fit well with the observations.

We further estimated the displacement and velocity distributions along time and obtained the maximum movement speed of 9.4 m/s as shown in Figure S5d. We aligned the East-West component seismic records at the ENH station with the origin time of the landslide by assuming a seismic wave propagation velocity of 3.35 km/s. The original broadband seismogram, 1 Hz high-pass filtered seismogram and 0.1 Hz low-pass filtered seismograms are shown in Figure S5a, b, and c, respectively. It could be observed that the long period seismic energy that is used in the landslide force history inversion fits almost perfectly with the landslide start time estimated from the inverted force history; however, it is hardly visible to the naked eye in the original broadband seismogram. High-frequency signal did not show up immediately after the occurrence of the event; instead, a small amplitude high-frequency wave-train appeared after the maximum velocity and a large amplitude high-frequency wave-train appeared very close to the end of the event, suggesting that the process generating the high-frequency seismic signals was not directly related to the main landslide movement. It should be noted that the arrival time of the high-frequency signals is not necessarily the occurrence time of the process generating the high-frequency signals since we assumed a seismic wave propagation velocity of 3.35 km/s to align the seismic records. The actual velocity of the high-frequency waves could be larger than our assumption, which could potentially make the arrival time earlier than the occurrence time of the process generating the high-frequency signals.

5. Discussion

The estimated mass for the Qianjiangping landslide is ~2.1655×10^{10} kg, which gives a sliding volume of ~1.08×10^{7} m^3, if we assume a density of 2.0×10^{3} kg/m^3. The estimated volume is ~54.14% of that obtained from the field survey [*Wang et al.*, 2008]. We can explain the mass discrepancy by analyzing the influence of mass mobilization and entrainment during sliding using a simple model. Figure S6a shows the shape of a simple slope, which results in constant accelerations for speed-up and slow-down phases as shown in Figure S6b. In realistic situations, mass mobilizations and entrainments occur very fast and the mobilized mass speed up to and the sliding mass slow down to an equivalent velocity during the process. To simplify calculation, we assume this process is instantaneous. In the model, 50% of the mass is from initial sliding and the other 50% is from mobilization and entrainment during sliding. We put the entrained mass at different locations from the beginning to the end to derive their

force and velocity distributions along the runout distance and evaluate their effects on the estimation of the sliding mass. In Figure S6, we use red, green, and blue dashed lines and solid circles to represent the estimated parameters when the entrained mass is located at runout distances of 0.2, 0.5, and 0.75, respectively.

We use the forces, which could be approximated using the inverted forces, and runout distances to estimate the sliding mass for each entrainment location. We first integrate the forces twice with respect to time and obtain their maximum values, which are shown as the dashed line in Figure 4a, and then divide them by runout distances, shown as the solid line in Figure 4a. From the estimated sliding mass shown in Figure 4b, it could be observed that if there was a mass entrainment event, wherever its location, the estimated mass would be smaller than the total mass. If the entrainment occurred at the slow-down stage (i.e., runout distance larger than 0.5), which frequently happens in reality, the estimated mass is no more than 60% of the total mass. We can use the estimated mass to derive velocity distributions and their maximum values and the estimated maximum velocities are 83.38% - 122.26% of actual maximum velocities as shown in Figure 4d.

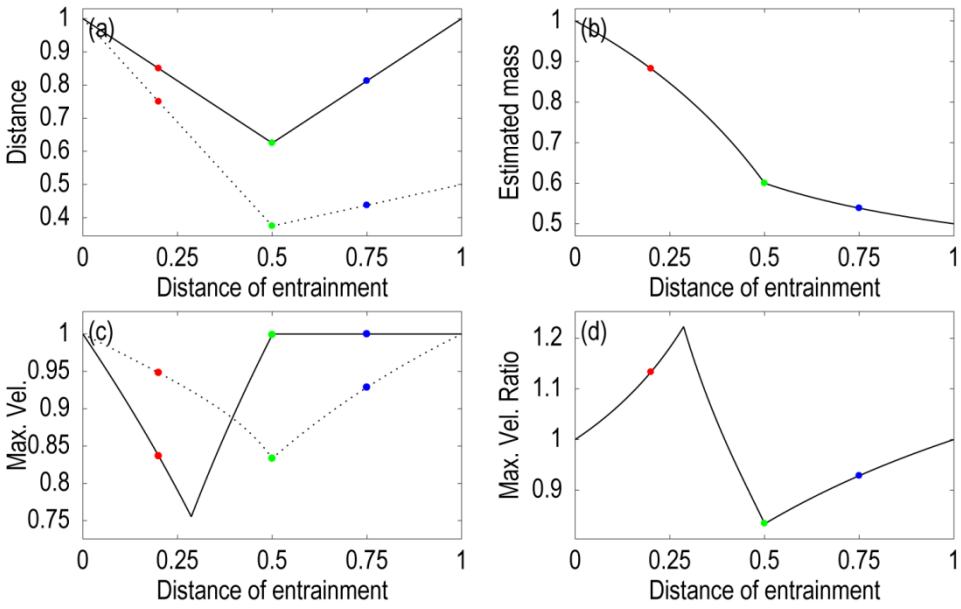

Figure 4. (a) real runout distances (solid line) and the maximum values of the integrations of the forces twice with respect to time (dashed line); (b) estimated mass for different entrainment location; (c) real (solid line) and estimated (dashed line) maximum velocities; (4) the ratio of the estimated maximum velocities to the real maximum velocities.

The above model calculations show that when the entrainment occurs in the slow-down phase, the estimated mass is far less than the total mass and is a closer approximation to the initial sliding mass. The forces in the slow-down phase show large amplitudes and short durations, which is in contrary to the predications of the sliding block model [*Zhao et al.*, 2015]. The inverted landslide force history for the

Xinmo landslide shows a shorter duration and larger amplitudes in the slow-down phase as compared with the force in the speed-up phase [*Z-y Li et al.*, 2019], suggesting that the landslide mobilized and entrained a large amount of pre-existing deposits during the slow-down phase, which is supported by field surveys [*Fan et al.*, 2017]. In addition, *Z-y Li et al.* [2019] estimated the Xinmo landslide trajectories using only the initial sliding volume of 4.46 million m^3, accounting for only ~34% of the total deposits (13 million m^3 [*Fan et al.*, 2017]), which is also consistent with the model calculations.

Seismically inferred total masses of two glacier collapses in western Tibet by *Kääb et al.* [2018] were underestimated by a factor of about 3-6 compared with the avalanche deposit volumes inferred from satellite images. The authors attributed this discrepancy to a significant decrease in mass before bulk material arrest due to progressive ice deposition along the path. However, an alternative explanation could be that the initial sliding mass was small and it mobilized and entrained a large amount of material during the slow-down phase. If the initial sliding mass was large, large forces in the initial stage should have been detected through the inversion. Mass mobilization and entrainment slow down the entire movement velocity; however, small slope angles and basal friction coefficients in the slow-down stage result in almost undetectable resistant forces, which lead to long runout distances. It could be inferred from the model calculations that the derived empirical relations between maximum inverted forces and sliding volumes may have systematic uncertainties, since the inverted force has a stronger relation with the initial sliding mass than the total deposit mass. Similarly, studies on landslide basal frictions based on landslide force inversion should carefully consider the influence of mass variations during sliding.

For the Qianjiangping landslide, field survey showed that the collapsed area was drawn down by the movement of the main sliding area and its sliding distance was very limited, suggesting that this part of mass did not participate in generating the seismically detected forces. This might be an explanation for the mass discrepancy. To find out when the draw-down occurred, we analyzed the high frequency seismic signals that occurred very close to the end of the landslide event. The East-West component broadband record at the ENH station, its S-transform [*Stockwell*, 2007; *Stockwell et al.*, 1996] spectrogram and the 1 Hz high-pass filtered record are shown in Figure S7. Since the amplitude in the later section is substantially larger than that in the earlier section, spectrograms of such signals are usually dominated by the large amplitude signals. We therefore normalized each time component of the spectrogram [*Huang et al.*, 2017]. The first part of the signal shows small amplitude with higher frequency, while the second part shows large amplitude with lower frequency and obvious wave dispersion, suggesting that they are body waves and surface waves produced by a rupture. With the help of the spectrogram and the high-pass filtered seismic record we estimated the times of the p phase, s phase, and surface-wave phase were 16:20:48.4, 16:21:4.2, and 16:21:7.2, respectively. The dominant frequency of the body waves was about 2 Hz, which is substantially lower than that of typical small earthquakes. The low frequencies of both body waves and surface wave signals and

the well-developed surface wave suggest that the rupture occurred on the earth surface. We estimated the epicentral distance and the occurrence time of the event to be 134.18 km and 16:20:26.4 assuming the P-wave velocity and S-wave velocity of 6.1 km/s and 3.55 km/s, respectively, suggesting that the event was a rupture on the earth surface during the landslide. We conjecture that the high-frequency seismic signal was generated when the draw-down occurred. The main sliding area mobilized the collapsed area shortly before it stopped, generating the high frequency seismic signal. And then, both of them stopped shortly after, resulting in a limited sliding distance of the collapsed area. Therefore, the estimated mass could be an approximation of the sliding mass in the main sliding area, which is smaller than total deposits.

6. Conclusions

A reasonable landslide force history inversion using long-period seismic records should meet two levels of requirements, i.e., mathematically correct and physically consistent. To obtain a physically consistent inversion result, the low frequency bound of the passband used in seismic data processing should have a period that is longer than the landslide duration. We propose an approach to determine the frequency band required by the inversion to reliably reconstruct landslide movement parameters from force-history inversion results. Based on the landslide force history inversion from long-period seismic waveform for the 2003 Qianjiangping landslide, we propose a simple model to study the effects of the initial sliding mass and the location of the mass entrainment on the seismically estimated sliding mass and other parameters. We conclude that if there is a mass entrainment, the seismically estimated mass is smaller than the total mass and if the entrainment occurs at the slow-down phase the seismically estimated mass is a closer approximation of the initial sliding mass.

Acknowledgements, Samples, and Data

The seismic data used in this study are from IRIS (https://www.iris.edu/hq/). The velocity model used in the inversion is derived from Crust1.0 (https://igppweb.ucsd.edu/~gabi/crust1.html). SAC software packages (http://ds.iris.edu/files/sac-manual/) were used for the seismic data processing. QSEIS06 (https://www.gfz-potsdam.de/) was used to calculate Green's Functions. This work was completed when the corresponding author was a visiting scholar at the University of Wyoming, which was financially supported by the China Scholarship Council under Grant 201904190026.

References

Allstadt, K. (2013), Extracting source characteristics and dynamics of the August 2010 Mount Meager landslide from broadband seismograms, *J. Geophys. Res. Earth Surf.*, *118*(3), 1472-1490, doi: 10.1002/jgrf.20110.

Brodsky, E. E., E. Gordeev, and H. Kanamori (2003), Landslide basal friction as

376 measured by seismic waves, *Geophys. Res. Lett.*, *30*(24), 2236, doi:
377 10.1029/2003GL018485.

378 Chao, W.-A., L. Zhao, S.-C. Chen, Y.-M. Wu, C.-H. Chen, and H.-H. Huang (2016),
379 Seismology-based early identification of dam-formation landquake events, *Sci. Rep.*,
380 *6*, 19259, doi: 10.1038/srep19259.

381 Dahlen, F. A. (1993), Single-force representation of shallow landslide sources, *Bull.*
382 *Seismol. Soc. Am.*, *83*(1), 130-143.

383 Ekström, G., and C. P. Stark (2013), Simple scaling of catastrophic landslide
384 dynamics, *Science*, *339*(6126), 1416-1419, doi: 10.1126/science.1232887.

385 Fan, X., Q. Xu, G. Scaringi, L. Dai, W. Li, X. Dong, X. Zhu, X. Pei, K. Dai, and H.-B.
386 Havenith (2017), Failure mechanism and kinematics of the deadly June 24th 2017
387 Xinmo landslide, Maoxian, Sichuan, China, *Landslides*, *14*(6), 2129-2146, doi:
388 10.1007/s10346-017-0907-7.

389 Fukao, Y. (1995), Single-force representation of earthquakes due to landslides or the
390 collapse of caverns, *Geophys. J. Int.*, *122*(1), 243-248, doi:
391 10.1111/j.1365-246X.1995.tb03551.x.

392 Gualtieri, L., and G. Ekström (2018), Broad-band seismic analysis and modeling of
393 the 2015 Taan Fjord, Alaska landslide using Instaseis, *Geophys. J. Int.*, *213*(3),
394 1912-1923, doi: 10.1093/gji/ggy086.

395 Hasegawa, H., and H. Kanamori (1987), Source mechanism of the magnitude 7.2
396 Grand Banks earthquake of November 1929: Double couple or submarine landslide?,
397 *Bull. Seismol. Soc. Am.*, *77*(6), 1984-2004.

398 Hibert, C., G. Ekström, and C. P. Stark (2014), Dynamics of the Bingham Canyon
399 Mine landslides from seismic signal analysis, *Geophys. Res. Lett.*, *41*(13), 4535-4541,
400 doi: 10.1002/2014GL060592.

401 Hibert, C., C. Stark, and G. Ekström (2015), Dynamics of the Oso-Steelhead landslide
402 from broadband seismic analysis, *Nat. Hazards Earth Syst. Sci.*, *15*(6), 1265-1273, doi:
403 10.5194/nhess-15-1265-2015.

404 Huang, X., Z. Li, D. Yu, Q. Xu, J. Fan, Z. Hao, and Y. Niu (2017), Evolution of a
405 giant debris flow in the transitional mountainous region between the Tibetan Plateau
406 and the Qinling Mountain range, Western China: Constraints from broadband seismic
407 records, *J. Asian Earth Sci.*, *148*, 181-191, doi: 10.1016/j.jseaes.2017.08.031.

408 Kääb, A., et al. (2018), Massive collapse of two glaciers in western Tibet in 2016 after
409 surge-like instability, *Nat. Geosci.*, *11*(2), 114-120, doi: 10.1038/s41561-017-0039-7.

410 Kanamori, H., and J. W. Given (1982), Analysis of long‐period seismic waves
411 excited by the May 18, 1980, eruption of Mount St. Helens—A terrestrial monopole?,
412 *J. Geophys. Res. Solid Earth*, *87*(B7), 5422-5432, doi: 10.1029/JB087iB07p05422.

413 Kanamori, H., J. W. Given, and T. Lay (1984), Analysis of seismic body waves
414 excited by the Mount St. Helens eruption of May 18, 1980, *J. Geophys. Res. Solid*

Earth, *89*(B3), 1856-1866, doi: 10.1029/JB089iB03p01856.

Li, W., Y. Chen, F. Liu, H. Yang, J. Liu, and B. Fu (2019), Chain-Style Landslide Hazardous Process: Constraints From Seismic Signals Analysis of the 2017 Xinmo Landslide, SW China, *J. Geophys. Res. Solid Earth*, *124*, 2025-2037, doi: 10.1029/2018JB016433.

Li, Z.-y., X.-h. Huang, D. Yu, J.-r. Su, and Q. Xu (2019), Broadband-seismic analysis of a massive landslide in southwestern China: Dynamics and fragmentation implications, *Geomorphology*, *336*, 31-39, doi: 10.1016/j.geomorph.2019.03.024.

Li, Z., X. Huang, Q. Xu, D. Yu, J. Fan, and X. Qiao (2017), Dynamics of the Wulong landslide revealed by broadband seismic records, *Earth Planets Space*, *69*(1), 27, doi: 10.1186/s40623-017-0610-x.

Moore, J. R., K. L. Pankow, S. R. Ford, K. D. Koper, J. M. Hale, J. Aaron, and C. F. Larsen (2017), Dynamics of the Bingham Canyon rock avalanches (Utah, USA) resolved from topographic, seismic, and infrasound data, *J. Geophys. Res. Earth Surf.*, *122*(3), 615-640, doi: 10.1002/2016JF004036.

Moretti, L., K. Allstadt, A. Mangeney, Y. Capdeville, E. Stutzmann, and F. Bouchut (2015), Numerical modeling of the Mount Meager landslide constrained by its force history derived from seismic data, *J. Geophys. Res. Solid Earth*, *120*(4), 2579-2599, doi: 10.1002/2014JB011426.

Moretti, L., A. Mangeney, Y. Capdeville, E. Stutzmann, C. Huggel, D. Schneider, and F. Bouchut (2012), Numerical modeling of the Mount Steller landslide flow history and of the generated long period seismic waves, *Geophys. Res. Lett.*, *39*(16), L16402, doi: 10.1029/2012GL052511.

Sheng, M., R. Chu, Y. Wang, and Q. Wang (2020), Inversion of Source Mechanisms for Single‐Force Events Using Broadband Waveforms, *Seismol. Res. Lett.*, *91*(3), 1820-1830, doi: 10.1785/0220190349.

Stockwell, R. G. (2007), A basis for efficient representation of the S-transform, *Digital Signal Processing*, *17*(1), 371-393, doi: 10.1016/j.dsp.2006.04.006.

Stockwell, R. G., L. Mansinha, and R. Lowe (1996), Localization of the complex spectrum: the S transform, *IEEE Trans. on Signal Processing*, *44*(4), 998-1001, doi: 10.1109/78.492555.

Wang, F., Y. Zhang, Z. Huo, X. Peng, S. Wang, and S. Yamasaki (2008), Mechanism for the rapid motion of the Qianjiangping landslide during reactivation by the first impoundment of the Three Gorges Dam reservoir, China, *Landslides*, *5*(4), 379-386, doi: 10.1007/s10346-008-0130-7.

Wang, R. (1999), A simple orthonormalization method for stable and efficient computation of Green's functions, *Bull. Seismol. Soc. Am.*, *89*(3), 733-741.

Yamada, M., H. Kumagai, Y. Matsushi, and T. Matsuzawa (2013), Dynamic landslide processes revealed by broadband seismic records, *Geophys. Res. Lett.*, *40*(12), 2998-3002, doi: 10.1002/grl.50437.

Yamada, M., A. Mangeney, Y. Matsushi, and L. Moretti (2016), Estimation of dynamic friction of the Akatani landslide from seismic waveform inversion and numerical simulation, *Geophys. J. Int.*, *206*(3), 1479-1486, doi: 10.1093/gji/ggw216.

Yamada, M., A. Mangeney, Y. Matsushi, and T. Matsuzawa (2018), Estimation of dynamic friction and movement history of large landslides, *Landslides*, *15*(10), 1963-1974, doi: 10.1007/s10346-018-1002-4.

Yu, D., X. Huang, and Z. Li (2020), Variation patterns of landslide basal friction revealed from long-period seismic waveform inversion, *Nat. Hazards*, *100*(1), 313-327, doi: 10.1007/s11069-019-03813-y.

Zhang, Z., S. He, and Q. Li (2020), Analyzing high-frequency seismic signals generated during a landslide using source discrepancies between two landslides, *Engineering Geology*, *272*, 105640, doi: 10.1016/j.enggeo.2020.105640.

Zhao, J., C. J. Ouyang, S. D. Ni, R. S. Chu, and A. Mangeney (2020), Analysis of the 2017 June Maoxian landslide processes with force histories from seismological inversion and terrain features, *Geophys. J. Int.*, *222*(3), 1965-1976, doi: 10.1093/gji/ggaa269.

Zhao, J., et al. (2015), Model space exploration for determining landslide source history from long-period seismic data, *Pure Appl. Geophys.*, *172*(2), 389-413, doi: 10.1007/s00024-014-0852-5.